Supplementary Information

High-Valent Manganese Promotes Percolating K-Vacancy Networks to Boost Bulk K^+ Conduction in $K_{2-\gamma}Mn_xFe_{4-x}O_{7-\delta}$

Zhungzhuang chen, Liping Li *, Taotao Huang, Junhong Zhou, Yaowen Wang, Xu Han, Yuhan Yi, and Guangshe Li *

State Key Laboratory of Inorganic Synthesis and Preparative Chemistry, College of Chemistry, Jilin University, Changchun 130012, P.R. China

***Corresponding authors.**

E-mail addresses: lipingli@jlu.edu.cn; guangshe@jlu.edu.cn

Supplementary Information:

Synthesis

Compositions $K_{2-\gamma}Mn_xFe_{4-x}O_{7-\delta}$ (x = 0, 0.4, 0.8, 1.2, 1.6, 2.0) were synthesized by an alkaline hydrothermal route using $Fe(NO_3)_3 \cdot 9H_2O$ (99%, Aladdin) and $Mn(NO_3)_2 \cdot 4H_2O$ (99%, Aladdin) at varied molar ratios in the presence of excess KOH(99%, Aladdin). Typically, 2.9 g of $Fe(NO_3)_3 \cdot 9H_2O$ and 1.8g of $Mn(NO_3)_2 \cdot 4H_2O$ were dissolved in 16 mL deionized water to afford a clear solution. To

efficiently add KOH without evaporating the solution's water content, the clear solution was stirred in an ice bath. During stirring, approximately 1 g of KOH was added every 3 – 5 minutes until 32 g KOH was incorporated. The mixture was transferred to a PTFE-lined stainless-steel autoclave and heated at 240 ° C for 20 h. Finally, the crystals of $K_{2-\gamma}Mn_xFe_{4-x}O_{7-\delta}$ were obtained. Crystals with other Mn contents were prepared by the same procedure while adjusting the $Fe(NO_3)_3 \cdot 9H_2O$ and $Mn(NO_3)_2 \cdot 4H_2O$ molar ratio. After cooling to room temperature, crystals were collected by filtration, washed with deionized water and dried in air at ambient temperature. The crystals are put into an agate ball-filled milling jar and ball-milled for 36 h at 360 rpm/min, using ethanol as the solvent. The obtained was dried in an oven at 75 ° C for 12 h。Subsequently, the fine powder was pressed into pellets with a diameter of 6 or 10 mm and a thickness of 0.05-0.2 cm. Finally, those pellets were sintered for 20 h at 600 ° C in an alumina crucible. The heating rate was 2 ° C /min, and the cooling rate was 5 ° C /min.

Characterization methods

The crystal structures of the $K_{2-\gamma}Mn_xFe_{4-x}O_{7-\delta}$ (x = 0, 0.4, 0.8, 1.2, 1.6, 2.0) electrolytes were examined by X-ray diffraction (XRD; Rigaku Miniflex) using a Cu Kα radiation source (λ = 1.5418 Å) at 40 kV and 15 mA in a scan range of 2θ between 10◦ to 90◦, with a 0.02◦ step size. The lattice parameters were calculated by Rietveld refinement on the GSAS program. The morphology and energy dispersive spectrometer (EDS) mapping of the samples were characterized using a field-emission scanning electron microscopy (SEM; Hitachi, JSM-6700F). The morphology of supports and catalysts was characterized by transmission electron microscopy (TEM, Tecnai G2S-Twin F20). X-ray photoelectron spectroscopy

(XPS) measurements were performed on an ESCALAB250 apparatus with a monochromatic Al Kα (1486.6 eV) X-ray source. All photoelectron peaks were calibrated by setting the binding energy of the contaminative carbon (C 1s) to 284.8 eV. Elemental compositions of the samples were obtained by inductively coupled plasma (ICP) on an Thermo, iCAP 7600. XAS measurements were performed on a laboratory device (easyXAFS300, easy-XAFS LLC), which is based on Rowland circle geometries with spherically bent crystal analyzers (SBCA) and a silicon drift detector. Si (5,5,3) and Ge (4,2,0) were used respectively to test for Fe K-edge. The Thermogravimetric Mass Spectrometry (TG-MS) was measured on the NETZSCH STA449F3 QMS403D \ Bruker V70 instrument, about 20 mg of the sample was heated from 25 °C to 600 °C at 10 °C·min-1 in a N_2 gas atmosphere. The Fourier Transform infrared spectroscopy (FT-IR) was detected under vacuum conditions by VERTEX 80V(Bruker). The electrochemical impedance spectroscopy (EIS) was recorded using Squidtat plus (Admiral) electrochemical work station in the frequency range from 2 MHz to 0.1 Hz at 30-300 ◦C. Their electronic conductivity was measured based on direct-current polarization method with a constant voltage of 0.1 V using Solartron 1260 and 1287 at room temperature. Before testing, the electrolyte pellets were polished with a polishing machine, and both surfaces of the pellets were sputtered with Pt as the blocking electrodes. All electrolyte pellets were preheated in a muffle furnace at 500°C for five hours. The electrochemical impedance spectroscopy and electronic conductivity were measured under a continuous flow of dry argon gas. All of impedance data are analyzed using Z-view software to determine the total resistance and grain boundary resistance.

Supplementary Figures and Tables:

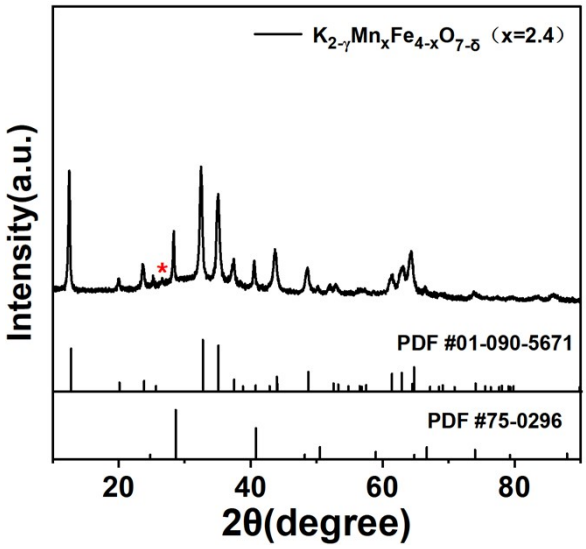

Fig. S1. XRD of $K_{2-\gamma}Mn_xFe_{4-x}O_{7-\delta}$ (x = 2.4). The symbol "*" represents an additional diffraction peak, indicating the formation of a secondary phase. High purity KCl (PDF #75-0296) was added as an internal standard.

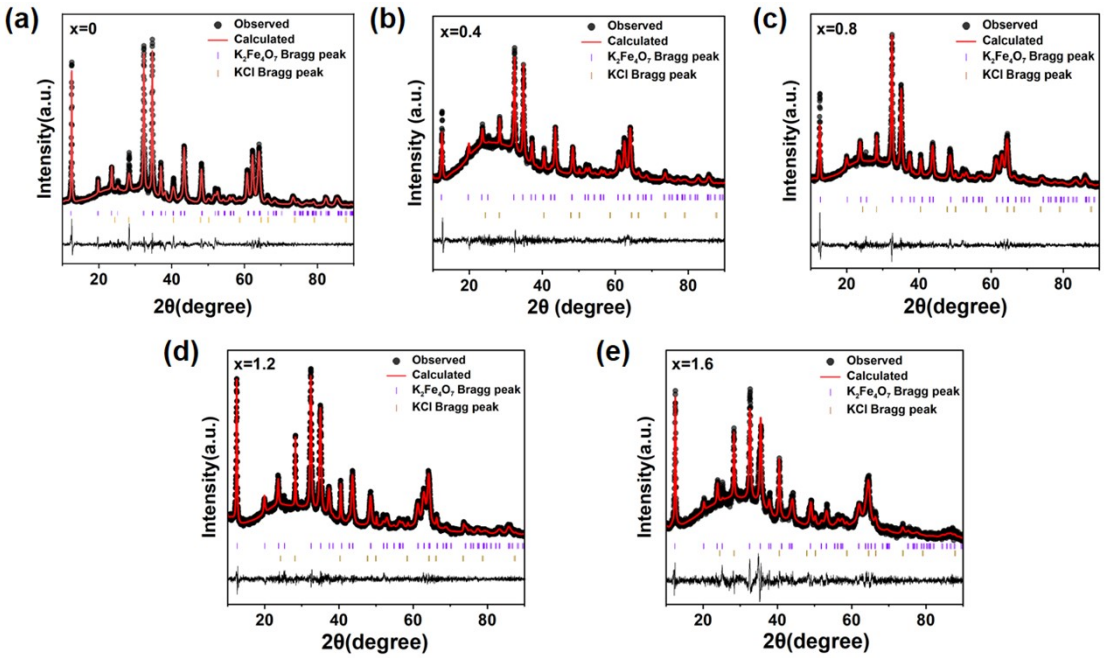

62

63 **Fig. S2.** XRD Rietveld refinement of $K_{2-\gamma}Mn_xFe_{4-x}O_{7-\delta}$ (x = 0, 0.4, 0.8, 1.2, 1.6): (a) x=0, (b) x=0.4, (c)
64 x=0.8, (d) x=1.2, (e) x=1.6 samples, respectively.

65

Table S1 Lattice parameters, XRD refinement factors of $K_{2-\gamma}Mn_xFe_{4-x}O_{7-\delta}$ (x = 0, 0.4, 0.8, 1.2, 1.6, 2.0).

x	Lattice parameters			Refinement factors		
	a (Å)	c (Å)	V (Å^3)	χ^2	R_{Wp}	R_p
0	5.164	7.024	162.3	1.08	0.068	0.051
0.4	5.145	7.036	161.3	1.06	0.061	0.046
0.8	5.136	7.024	160.5	1.10	0.062	0.047
1.2	5.117	7.034	159.6	0.85	0.059	0.045
1.6	5.114	7.044	159.5	0.86	0.057	0.044
2.0	5.116	7.027	159.3	0.87	0.060	0.047

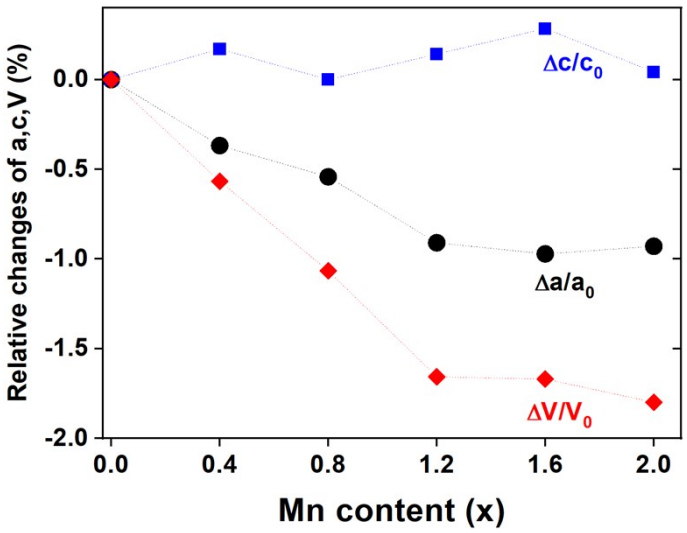

Fig. S3 Relative changes of lattice parameters *a, c,* and unit cell volume *V* of $K_{2-\gamma}Mn_xFe_{4-x}O_{7-\delta}$. Δ a=$a$-$a_0$, Δ c=c-c_0, and ΔV=V-V_0, where, a_0, c_0 and V_0 are the values of x=0.

73 **Table S2.** Element content (in mole ratio) obtained from ICP analysis.

74

x	**K**	**Mn**	**Fe**	**Calculated value of γ in the molecular formula $K_{2-\gamma}Mn_xFe_{4-x}O_{7-\delta}$**
0	1.46	0	4.00	0.54
0.4	1.08	0.40	3.60	0.92
0.8	0.96	0.79	3.21	1.08
1.2	0.83	1.05	2.95	1.17
1.6	0.81	1.52	2.48	1.19
2.0	0.75	1.97	2.03	1.25

75

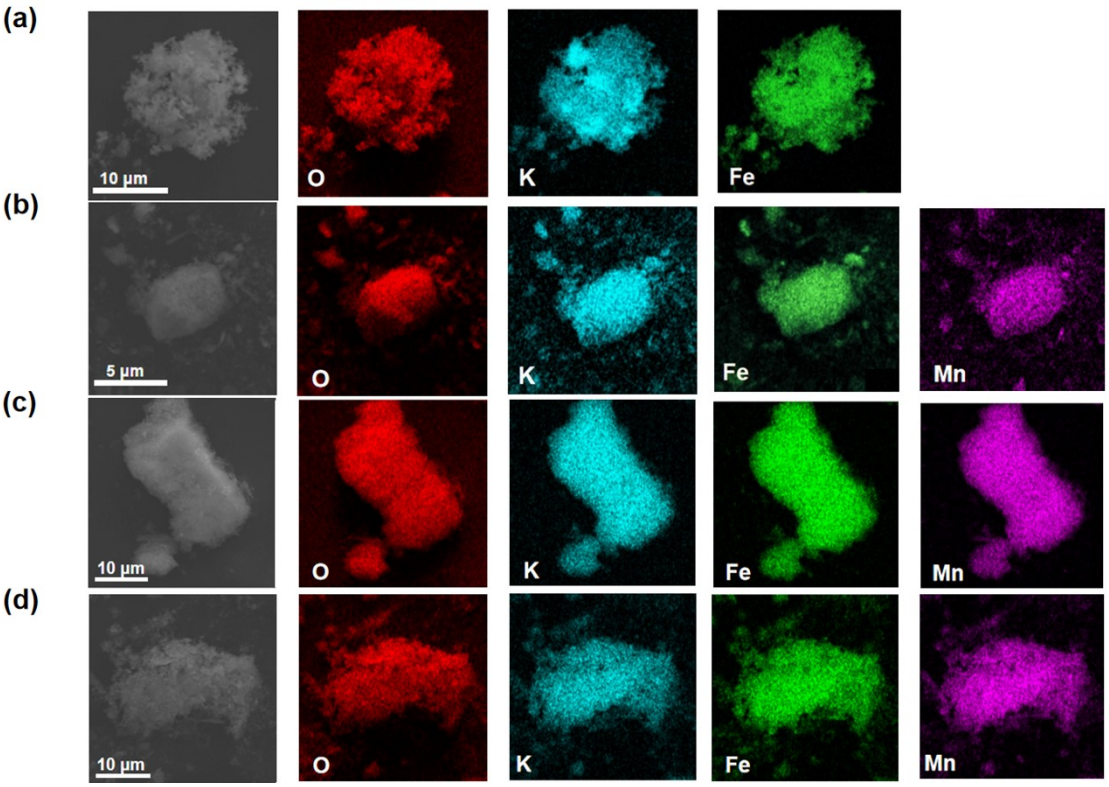

Fig. S4. EDS elements distribution mappings of $K_{2-\gamma}Mn_xFe_{4-x}O_{7-\delta}$: (a) x = 0, (b) x = 0.8 (c) x=1.6 and (d) x = 2.0

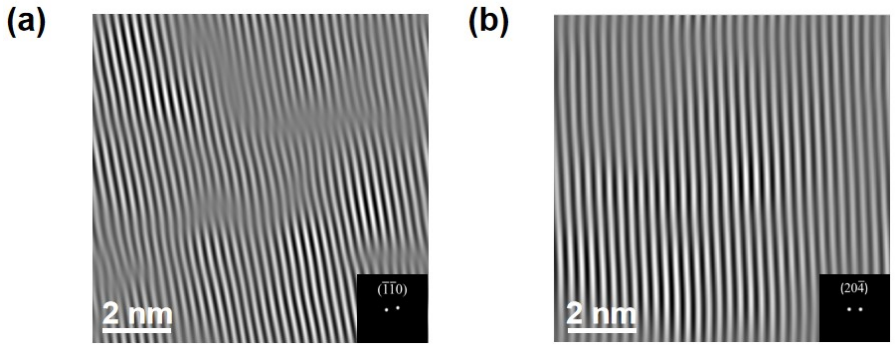

Fig. S5. IFFT patterns of the $(\bar{1}\bar{1}0)$ and $(20\bar{4})$ crystal planes in the selected regions Ⅰ and Ⅱ of $K_{2-\gamma}Mn_xFe_{4-x}O_{7-\delta}$: (a) x = 0, (b) x = 2.0.

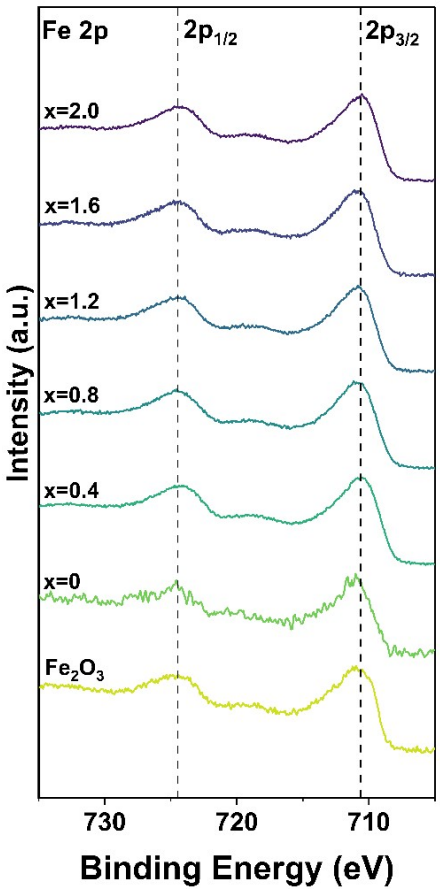

83

84 **Fig. S6.** Fe 2p XPS spectra of. $K_{2-\gamma}Mn_xFe_{4-x}O_{7-\delta}$ samples (x = 0.4, 0.8, 1.2, 1.6, 2.0) and Fe_2O_3.

85

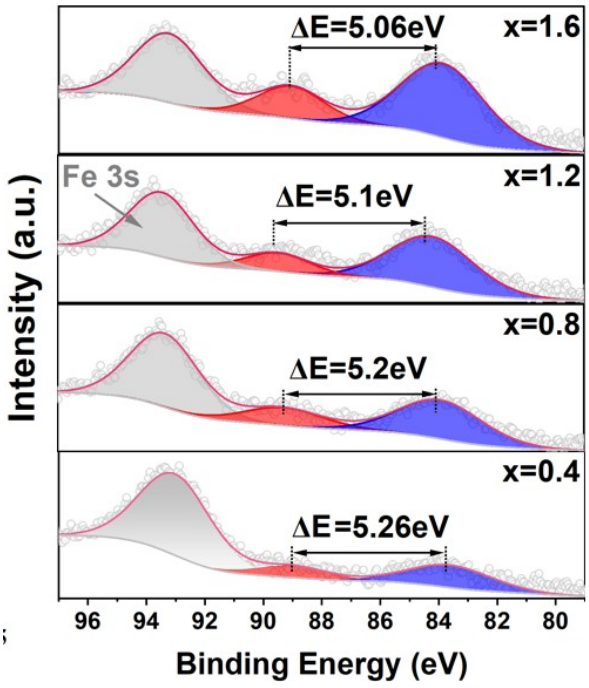

86

87 **Fig. S7.** Mn 3s XPS spectra of. $K_{2-\gamma}Mn_xFe_{4-x}O_{7-\delta}$ samples (x = 0.4, 0.8, 1.2 ,1.6)**.**

88

89 **Table S3.** Oxidation states of Mn in $K_{2-\gamma}Mn_xFe_{4-x}O_{7-\delta}$ (x = 0.4, 0.8, 1.2, 1.6, 2.0).

x	**Mn oxidation state** $Average\ Valence = 8.95 - 1.13 \times \Delta E$
0.4	+3.01
0.8	+3.07
1.2	+3.19
1.6	+3.23
2.0	+3.32

90

91

92

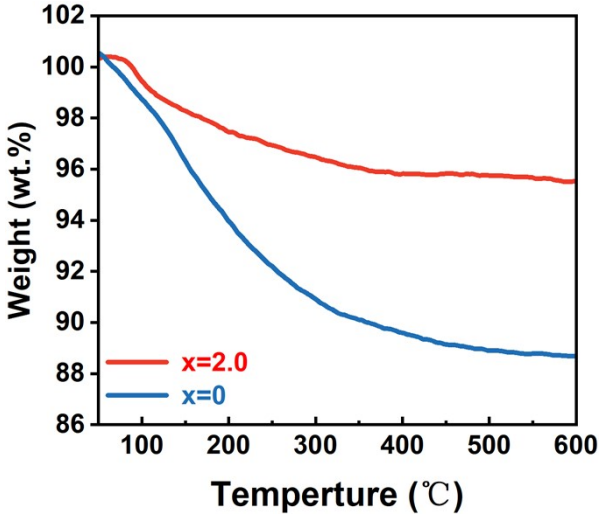

93

94 **Fig. S8.** TGA of $K_{2-\gamma}Mn_xFe_{4-x}O_{7-\delta}$ (x = 0) and (x = 2.0), respectively.

95

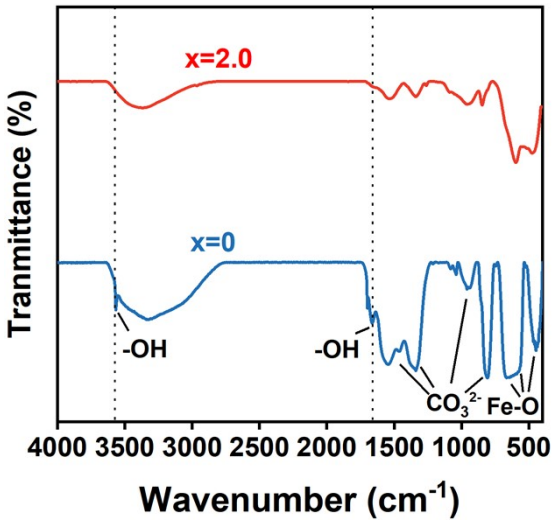

96

97 **Fig. S9.** FTIR spectra of $K_{2-\gamma}Mn_xFe_{4-x}O_{7-\delta}$ (x = 0) and (x = 2.0), respectively. Key absorption bands are

98 assigned according to Reference [1], corresponding to hydroxyl (OH) and carbonate (CO_3^{2-}) group peaks

99 and to Fe-O modes.

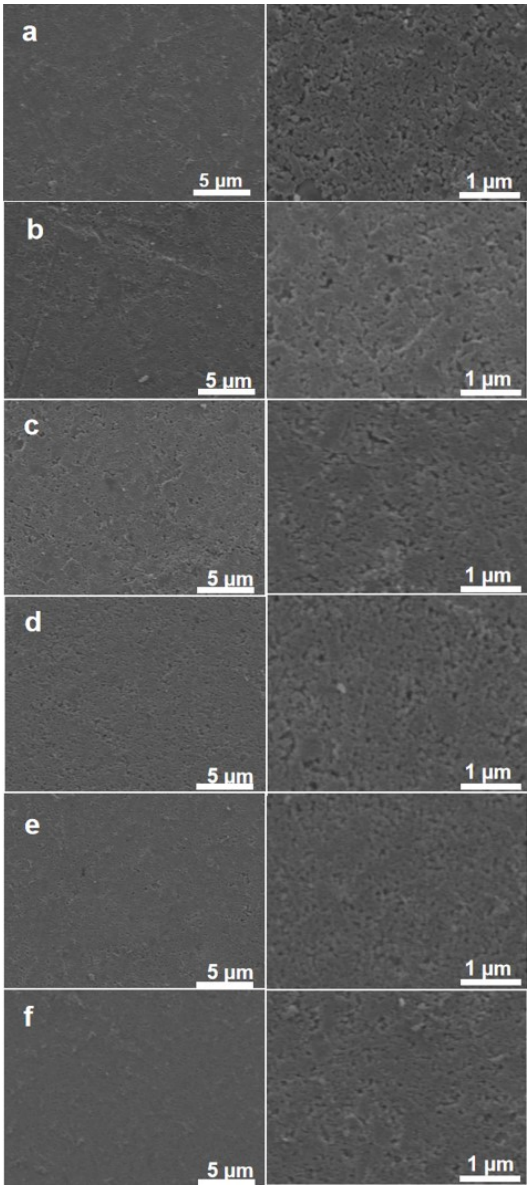

Fig. S10. SEM images of polished solid electrolyte $K_{2-\gamma}Mn_xFe_{4-x}O_{7-\delta}$ (a) x = 0, (b) x = 0.4, (c) x = 0.8, (d) x = 1.2, (e) x = 1.6, (f) x = 2.0.

Table S4. Dimensions, theoretical density (ρ_{theor}), apparent density (ρ_{exp}), and relative density ratio (ρ_{exp}/ρ_{theor}) of as-synthesized $K_{2-\gamma}Mn_xFe_{4-x}O_{7-\delta}$ (x = 0, 0.4, 0.8, 1.2, 1.6, 2.0) pellets for AC impedance measurements.

x	**Mass (g)**	**Diameter (cm)**	**Thickness (cm)**	**ρ_{theor} [a] ($g \cdot cm^{-3}$)**	**ρ_{exp} [b] ($g \cdot cm^{-3}$)**	**ρ_{exp}/ρ_{theor} (%)**
0	0.066	0.589	0.073	3.973	3.318	83.5
0.4	0.058	0.580	0.070	3.837	3.136	81.7
0.8	0.054	0.575	0.065	3.804	3.199	84.1
1.2	0.060	0.590	0.068	3.773	3.227	85.5
1.6	0.056	0.580	0.065	3.762	3.260	86.6
2.0	0.048	0.560	0.062	3.738	3.143	84.1

[a] ρ_{theor} value is calculated by the formula $\rho_{theor} = \frac{ZM}{V_{cell}N_A}$, where Z represents the quantity of atoms within a unit cell, M is the total mass of those atoms in one unit cell, V_{cell} stands for the unit cell's volume and N_A denotes Avogadro's constant.

[b] ρ_{exp} value is calculated by the formula $\rho_{exp}=m/V$, where m stands for the mass of ceramic pellet examined, and V for its volume which can be determined by the area and thickness of the ceramic pellet.

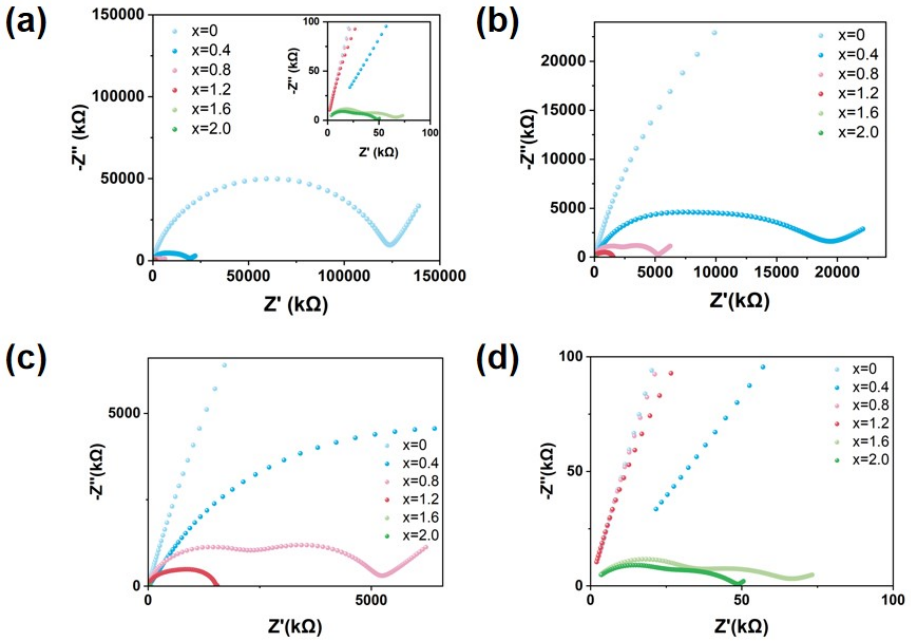

Fig. S11. Room-temperature Nyquist impedance plot of $K_{2-\gamma}Mn_xFe_{4-x}O_{7-\delta}$ (x = 0 0.4, 0.8, 1.2, 1.6, 2.0) and local enlargements of impedance details from samples with varying concentrations.

Table S5. The fitted resistance, CPE parameters and the corresponding capacitances of $K_{2-\gamma}Mn_xFe_{4-x}O_{7-\delta}$ (x = 0 0.4, 0.8, 1.2, 1.6, 2.0) by fitting the equivalent circuit consisted of R_1-CPE_1 in parallel, R_2-CPE_2 in parallel, and W_1 in series.

x	R_1(k Ω)	CPE_1(F)	C_1(F)	R_2(k Ω)	CPE_2(F)	C_2(F)
0	5.03×10^{4}	5.48×10^{-11}	2.18×10^{-11}	9.50×10^{4}	5.95×10^{-10}	3.24×10^{-10}
0.4	4.89×10^{3}	6.04×10^{-11}	2.95×10^{-11}	1.39×10^{4}	1.30×10^{-9}	1.07×10^{-10}
0.8	2.16×10^{3}	4.05×10^{-11}	1.33×10^{-11}	2.94×10^{3}	1.22×10^{-9}	2.73×10^{-10}
1.2	5.79×10^{2}	5.80×10^{-11}	1.68×10^{-11}	9.47×10^{2}	2.65×10^{-9}	1.04×10^{-9}
1.6	28.5	6.68×10^{-10}	2.50×10^{-11}	35.4	4.71×10^{-7}	4.24×10^{-9}
2.0	19.9	6.84×10^{-10}	2.31×10^{-11}	28.8	2.03×10^{-7}	1.06×10^{-9}

Table S6. Room-temperature ionic conductivities of solid electrolytes $K_{2-\gamma}Mn_xFe_{4-x}O_{7-\delta}$ (x = 0 0.4, 0.8, 1.2, 1.6, 2.0).

x	R_b（kΩ）	R_{gb}（kΩ）	σ_b（S·cm^{-1}）	σ_{gb} （S·cm^{-1}）	σ_{total}（S·cm^{-1}）
0	5.03×10^{4}	9.50×10^{4}	5.32×10^{-9}	2.82×10^{-9}	1.84×10^{-9}
0.4	4.89×10^{3}	1.39×10^{4}	5.42×10^{-8}	1.90×10^{-8}	1.41×10^{-8}
0.8	2.16×10^{3}	2.94×10^{3}	1.15×10^{-7}	8.51×10^{-8}	4.91×10^{-8}
1.2	5.79×10^{2}	9.47×10^{2}	4.29×10^{-7}	2.62×10^{-7}	1.63×10^{-7}
1.6	28.5	35.4	8.63×10^{-6}	6.95×10^{-6}	3.85×10^{-6}
2.0	19.9	28.8	1.26×10^{-5}	8.74×10^{-6}	5.17×10^{-6}

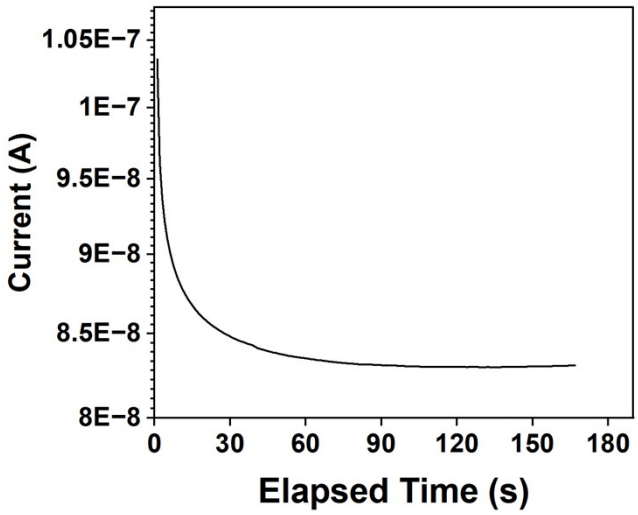

127

128 **Fig. S12.** Direct-current (DC) polarization with blocking electrodes of $K_{2-\gamma}Mn_xFe_{4-x}O_{7-\delta}$ (x = 2.0) under

129 inert gas.

130

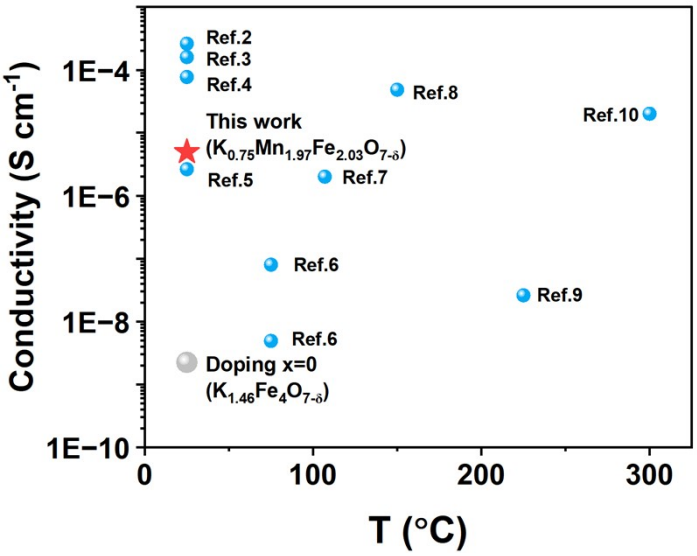

131

132 **Fig. S13.** A comprehensive comparison of reported solid-state electrolytes for potassium-ion batteries

133 and their intrinsic potassium-ion conductivities. Red stars denote data for the Mn-doped sample with x

134 = 2.0 from this work, gray spheres represent the undoped samples, and blue spheres correspond to solid-

135 state potassium-ion electrolytes reported in the references [2-10].

136

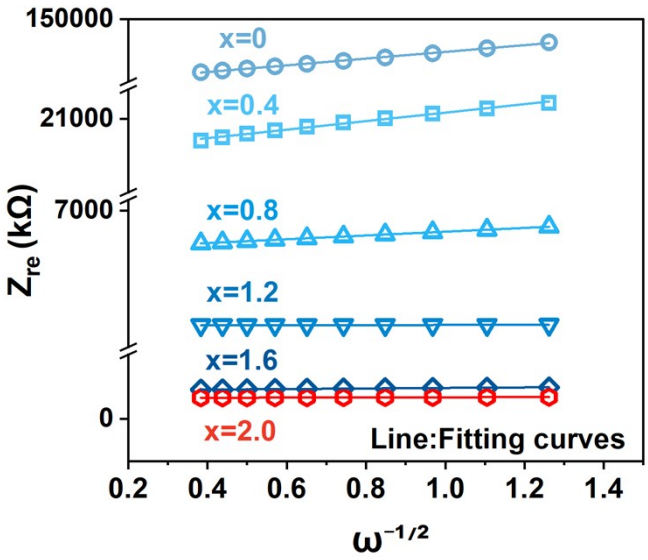

Fig. S14. Real part of impedance (Z_{re}) vs. $\omega^{-1/2}$ for $K_{2-\gamma}Mn_xFe_{4-x}O_{7-\delta}$ (x = 0 0.4, 0.8, 1.2, 1.6, 2.0), where the Warburg coefficients (σ_W) is obtained from linear fitting.

142 **Table S7.** The computed Warburg factors (σ_w) and K^+ diffusion coefficient of (D_{K+}) of the $K_{2-\gamma}Mn_xFe_{4-x}O_{7-\delta}$ (x = 0 0.4, 0.8, 1.2, 1.6, 2.0).

144

x	σ_w (Ω $s^{-1/2}$)	D_{K+} (cm^2 s^{-1})
0	1.61×10^{7}	1.8×10^{-23}
0.4	2.89×10^{6}	9.4×10^{-22}
0.8	9.04×10^{5}	9.7×10^{-20}
1.2	1.76×10^{4}	4.0×10^{-17}
1.6	6130	3.5×10^{-16}
2.0	1770	4.8×10^{-15}

145

References

[1] F. Dai, Q. Zhuang, G. Huang, H. Deng and X. Zhang, ACS Omega, 2023, 8, 17064-17076.

[2] A. Haffner, A.-K. Hatz, O. E. O. Zeman, C. Hoch, B. V. Lotsch, D. Johrendt, Angew. Chem. Int. Ed. 2021, 60, 13641.

[3] X. Zhang, B. Yi, W. Jia, S. Zhao, S. Savilov, S. Yao, Z. X. Shen, G. Chen, Z. Wei, F. Du, Angew. Chem. Int. Ed., 2025, 64, e202413214.

[4] J. Shao, J. Zheng, L. Qin, S. Zhang, Y. Ren, Y. Wu, Angew. Chem. Int. Ed. 2022, 61, e202200606; Angew. Chem. 2022, 134, e202200606.

[5] G.-G. Zhang, P. Qiu, J.-X. Kang, Z. Lu, A.-Q. Zhu, X. Yu, et al. Inorg. Chem. Front., 2024,11, 8715-8724.

[6] H. Ben Yahia, K. Motohashi, H. Ishibashi, Y. Kubota, A. Kosuga, A. Sakuda, et al. The Journal of Physical Chemistry C, 2024, 128, 8900-8910.

[7] Y. Sadikin, R. V. Skoryunov, O. A. Babanova, A. V. Soloninin, Z. Lodziana, M. Brighi, et al. The Journal of Physical Chemistry C, 2017, 121, 5503-5514.

[8] Jiang Wang, Gangtie Lei, Teng He, Hujun Cao, Ping Chen, Journal of Energy Chemistry, 2022, 69, 555-560.

[9] M. Jørgensen, S. R. H. Jensen, T. D. Humphries, M. R. Rowles, M. V. Sofianos, C. E. Buckley, et al. The Journal of Physical Chemistry C, 2020, 124, 11340-11349.

[10] E. Wang and M. Greenblatt, Chemistry of Materials, 1991, 3, 542-546.